

## Nuclear resonance fluorescence excitations near 2 MeV in $^{235}\text{U}$ and $^{239}\text{Pu}$

W. Bertozzi,<sup>1</sup> J. A. Caggiano,<sup>2</sup> W. K. Hensley,<sup>2</sup> M. S. Johnson,<sup>3</sup> S. E. Korbly,<sup>1</sup> R. J. Ledoux,<sup>1</sup> D. P. McNabb,<sup>3</sup> E. B. Norman,<sup>3</sup>  
W. H. Park,<sup>1</sup> and G. A. Warren<sup>2</sup>

<sup>1</sup>Passport Systems Incorporated, Acton, Massachusetts 01720, USA

<sup>2</sup>Pacific Northwest National Laboratory, Richland, Washington 99352, USA

<sup>3</sup>Lawrence Livermore National Laboratory, Livermore, California 94550, USA

(Received 30 June 2008; published 8 October 2008)

A search for nuclear resonance fluorescence excitations in  $^{235}\text{U}$  and  $^{239}\text{Pu}$  within the energy range of 1.0- to 2.5-MeV was performed using a 4-MeV continuous bremsstrahlung source at the High Voltage Research Laboratory at the Massachusetts Institute of Technology. Measurements utilizing high purity Ge detectors at backward angles identified nine photopeaks in  $^{235}\text{U}$  and 12 photopeaks in  $^{239}\text{Pu}$  in this energy range. These resonances provide unique signatures that allow the materials to be nonintrusively detected in a variety of environments including fuel cells, waste drums, vehicles, and containers. The presence and properties of these states may prove useful in understanding the mechanisms for mixing low-lying collective dipole excitations with other states at low excitations in heavy nuclei.

DOI: [10.1103/PhysRevC.78.041601](https://doi.org/10.1103/PhysRevC.78.041601)

PACS number(s): 23.20.Lv, 25.60.Dz, 25.20.Dc, 27.90.+b

*Introduction.* In the current geopolitical environment, proliferation of nuclear and radiological materials is a major concern. Many efforts are underway to develop a system that can rapidly identify and characterize illicit nuclear and radiological materials. One class of such systems takes advantage of the naturally emitted radiation of radiological material to passively detect their intrinsic signatures. Unfortunately, these signals can be limited by shielding effects. Other classes of systems take an “active” approach and use photons, neutrons, or muons (see Refs. [1–5]) to probe containers of interest. These systems utilize external radiation sources to stimulate the material within the container and detect the resulting signals to infer the material composition.

Nuclear resonance fluorescence (NRF) provides a unique approach to study nuclear isotopes. NRF is a phenomenon in which a high-energy photon excites a nucleus to a higher level that subsequently decays to a lower lying level by emitting a  $\gamma$  ray of energy equal to the energy difference between the resonance level and lower-lying level. This process is analogous to atomic fluorescence where photons excite an atomic-bound electron to a higher energy level. The resonant energies in NRF are in the 1 to 10 MeV range. As a result, the attenuation path-lengths for NRF photons are much longer than x-ray photons and thermal neutrons used in other assay techniques, allowing the technique to work through many inches of lead or steel or several feet of hydrogenous material.

As a research tool, NRF has been used to probe collective excitations in deformed rare-earth and actinide nuclei (Refs. [6,7] and references therein). Two collective modes have been established at energies below 3 MeV. One mode is the so-called scissors-mode, which has been observed in even-even rare earth and actinide nuclei [8]. In the scissors-mode, the proton and neutron distributions oscillate about their respective center-of-mass and between their respective major axes, giving a scissors-like motion (see Ref. [9]). This mode is a magnetic dipole excitation. The second collective mode is an octupole-quadrupole excitation, where the excitation consists of an admixture of octupole and quadrupole vibrations. This

mode is an electric dipole excitation. Other modes are possible but these are the major ones that have been identified in the literature.

This paper describes the measurement of NRF excitations in  $^{235}\text{U}$  and  $^{239}\text{Pu}$ . These resonances offer opportunities to use the NRF technique for nonintrusive inspection and study the nuclear structure of even-odd actinides. This report describes the initial set of measurements determining the locations and strengths of the NRF states in  $^{235}\text{U}$  and  $^{239}\text{Pu}$ .

*Experimental method.* Measurements of NRF states in  $^{235}\text{U}$  and  $^{239}\text{Pu}$  were conducted using the  $(\gamma, \gamma')$  reaction with bremsstrahlung photons. The cross sections of NRF states in  $^{235}\text{U}$  and  $^{239}\text{Pu}$  were determined by comparing transition intensities in  $^{235}\text{U}$  and  $^{239}\text{Pu}$  to simultaneously measured intensities of materials with known cross sections. The normalizing materials were chosen such that the  $\gamma$ -ray energy was within  $\sim 100$  keV of the observed  $\gamma$ -ray transitions in  $^{235}\text{U}$  and  $^{239}\text{Pu}$ .

The setup for this experiment, depicted in Fig. 1, was designed and constructed by Passport Systems Inc. as part of a test-bed for NRF experiments at the 4 MeV Van de Graaff electron accelerator at the High Voltage Research Laboratory (HVRL) at the Massachusetts Institute of Technology (MIT).

Bremsstrahlung photons were produced by impinging an electron beam onto a “radiator” consisting of 102- $\mu\text{m}$  Au backed by 1-cm Cu (used for cooling and electron cleanup). The radiator was electrically isolated and the average beam current was recorded. The bremsstrahlung photons immediately pass through a 20-cm long lead collimator with a 2.5° half angle, conical opening. Additional shielding was placed around the radiator to reduce background. The photon beam was aligned by steering the electron beam on the radiator and observing the x-ray image with a Perkin-Elmer imager downstream of the target (not shown Fig. 1). The NRF targets were placed 50 to 70 cm from the radiator (D1 in Fig. 1) and the entire target was completely illuminated by the bremsstrahlung photons. The normalizing material was either placed directly in front of the target or directly behind it. Measurements of

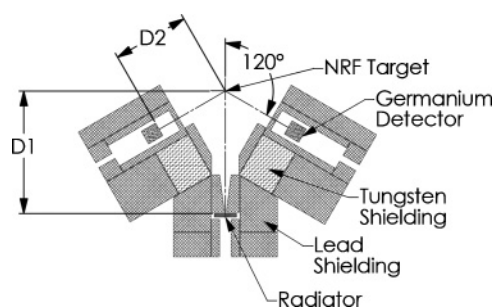


FIG. 1. NRF setup at the HVRL at MIT. See text for details.

$^{235}\text{U}$  used an end-point energy of 2.2 MeV and  $^{239}\text{Pu}$  used 2.8 MeV. Total integrated charge of 0.47 and 1.65 C were used for  $^{235}\text{U}$  and  $^{239}\text{Pu}$ , respectively.

The  $^{235}\text{U}$  target consisted of 220 grams of thin uranium metal foils placed inside a polyethylene terephthalate (PET) container. The uranium was enriched to 93%  $^{235}\text{U}$ . PET was chosen as the container material because of its low average atomic number and the absence of NRF resonances below 2.8 MeV. The uranium foils were arranged within the 3.5 in. inner diameter container so that the material was as close to uniform thickness as possible. Analysis of the x-ray images of the  $^{235}\text{U}$  target determined that the thickness varied from roughly 1.5 to 2.5 mm with an average of 1.9 mm. Uncertainties arising from this variation are accounted for in the cross section uncertainties. A manganese foil, 4.8 mm thick and the same diameter as the  $^{235}\text{U}$  target, provided NRF lines for calibration.

The Pu targets each contained approximately 4 grams of  $\sim 93\%$   $^{239}\text{Pu}$ . Each Pu target was 1.5 cm in diameter, 1.5 mm thick, and was encapsulated in 25 grams of Nitronic-40 with a 1-mil stainless steel window. The manganese of the Nitronic-40 (and other elements) did produce extraneous photopeaks, which served as an energy calibration. The outer diameter of the Nitronic-40 holder was approximately 2.5 cm. For normalization, thin disks of Al (approximately 1.2 mm thick and 1.6 cm in diameter) were placed directly in front of the Pu target.

Two different target configurations were used during the Pu measurements. In the first, a single target with no Al normalizer was used at the center of the bremsstrahlung beam. In the second configuration, two Pu targets, with Al normalizers, were used side-by-side separated by approximately 1 cm and centered in the beam. The additional target increased the counting rate by a factor of 2. The  $\gamma$ -ray flux distribution over this spatial range was studied with MCNP [10] and found to be flat, which was consistent with the online x-ray images. The Pu histogram in Fig. 3 includes data from both target configurations. However, the results given in Table I are generated from the two-target configuration with the Al normalizers in place.

The scattered  $\gamma$  rays were measured with two HPGe detectors at 40 to 50 cm from the target (D2 in Fig. 1), and  $\pm 120^\circ$  with respect to the beam direction. Both detectors were encased in thick Pb shielding to reduce background and collimated to view only the NRF target. The openings to the detectors were covered with Pb absorbers of various

TABLE I. Results from significant  $\gamma$ -ray transitions associated with  $^{235}\text{U}$  and  $^{239}\text{Pu}$ . Given in the table are isotope, transition energies, statistical significance, and cross sections. The daggers and asterisks are explained in the text.

Isotope	Transition (keV)	Statistical significance	Cross section (eV·b)
$^{235}\text{U}$	1656.23(80)	5.8	4.1(13)
	1687.26(33) <sup>†</sup>	10.2	6.1(11)
	1733.60(22) <sup>†</sup>	56.4	29.8(39)
	1769.16(28) <sup>‡</sup>	9.3	4.4(10)
	1815.31(22) <sup>‡</sup>	19.9	9.7(17)
	1827.54(23)	13.3	6.7(12)
	1862.31(20)	20.1	9.6(17)
	2003.32(25)	14.5	9.7(17)
	2006.19(31)	7.2	4.7(16)
	$^{239}\text{Pu}$	2040.25(21)	5.8
2046.89(31)		4.2	5(2)
2135.00(37)*		3.5	4(2)
2143.56(13)*		9.7	13(2)
2150.98(31)*		4.2	5(2)
2289.02(25)		6.2	8(2)
2423.48(22)**		7.2	10(2)
2431.66(25)**		6.3	9(3)
2454.37(26)		6.2	9(3)
2460.46(37)		4.7	6(4)
2464.60(30)		5.7	8(4)
2471.07(34)		4.6	6(2)

thicknesses (e.g. 3/4 in. and 1 in.) to reduce dead time at various end-point energies. For the HEU measurements with a 1 in. absorber in front of the two detectors, the data acquisition rate was 3.2 kHz and 4.0 kHz with a dead time of 5.5% and 9.1%. For the Pu measurements, the first configuration had a data acquisition rate of about 600 Hz for each detector with a dead time rate of 1–2% with a 1 in. absorber, and the second configuration had a 5 kHz data rate with a dead time of 17% for a 3/4 in. absorber.

**Results.** Spectra from measurements of the HEU+Mn+PET container and Mn only are shown in Fig. 2. Measurements were conducted on the PET container alone to confirm that the container contributed no peaks in this energy range. Additional measurements were conducted with the HEU sample in place but without the beam to confirm that only the 1764 keV from  $^{214}\text{Bi}$  could be attributed to the passive radiological decay of the HEU and room background. In the energy range shown, background states from  $^{214}\text{Bi}$  radioactive decay as well as the  $^{55}\text{Mn}$  NRF states at 1758 and 1884 keV were observed. The 1884-keV resonant line of  $^{55}\text{Mn}$  was used as a reference line to calibrate the  $^{235}\text{U}$  cross sections. The remaining peaks are attributed to  $^{235}\text{U}$ . The next likely source of NRF peaks would be from the 7% of  $^{238}\text{U}$  in the HEU sample. However, these peaks are known [7] and are inconsistent with the observed peaks.

The histogram for  $^{239}\text{Pu}$  is shown in Fig. 3. Several peaks are  $\gamma$ -ray transitions from NRF states in the Al normalizer and  $^{55}\text{Mn}$ ,  $^{53}\text{Cr}$ , and  $^{57}\text{Fe}$  of the Nitronic-40 holder, as evident in the lower (background) histogram in Fig. 3. It is possible

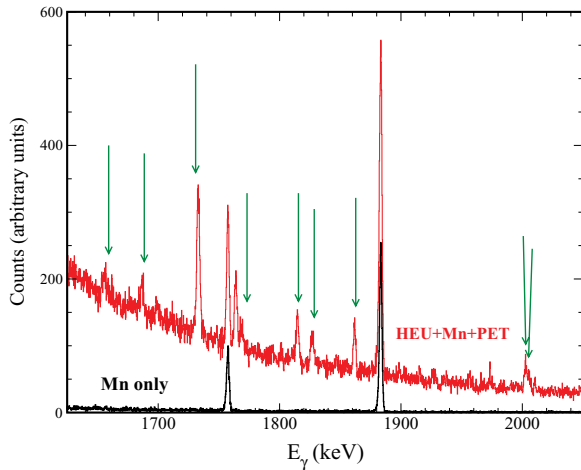


FIG. 2. (Color online) Histograms of the measured spectra for the  $^{235}\text{U}$  measurements. The top spectrum is for the HEU+Mn+PET plastic container. Arrows indicate peaks attributed to  $^{235}\text{U}$ . The bottom spectrum is for Mn only. The relative scale of the Mn only spectrum to the HEU+Mn+PET spectrum is arbitrary. The peak at 1764 keV not attributed to Mn or  $^{235}\text{U}$  is from  $^{214}\text{Bi}$  radioactive decay.

that one or more peaks are very strong NRF states from the other isotopic components of the Pu target, but it is assumed here that since  $\sim 93\%$  of the target is  $^{239}\text{Pu}$ , the peaks are most likely from  $^{239}\text{Pu}$ . Because of low statistics a smooth curve is overlaid on both histograms to aid the eye. The 2211-keV line is a resonance in  $^{27}\text{Al}$  and was used as a reference to calibrate the  $^{239}\text{Pu}$  cross sections.

Listed in Table I are the measured isotopes, transition energies, statistical significance, and cross sections. The energies in Table I were determined from energy calibrations of neighboring contaminant peaks. The column labeled as statistical significance gives the ratio of the counts in a

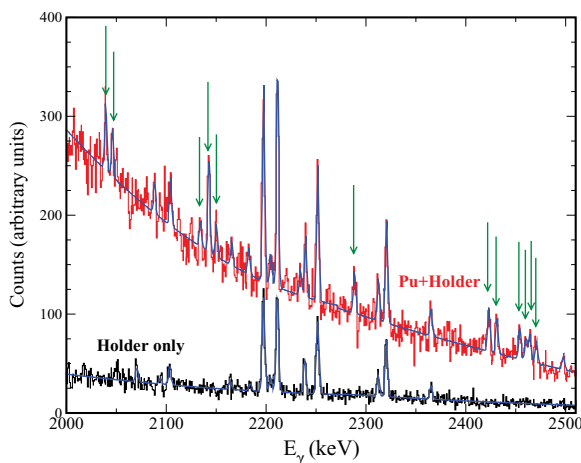


FIG. 3. (Color online) Histograms of the measured spectra for the  $^{239}\text{Pu}$  measurements. The upper histogram is a compilation of two data runs in two different configurations (Pu target and holder). The lower histogram is the background (holder only) spectrum from one run. Both data sets include Al calibration target. The arrows indicate peaks attributed to  $^{239}\text{Pu}$ . A smooth curve is overlaid on both histograms to aid the eye.

measured peak to the statistical and systematic uncertainties added in quadrature. Only peaks with a statistical significance greater than 4.0 were assigned to their respective isotopes in Table I with the exception of one photopeak at 2135 keV in the  $^{239}\text{Pu}$  data set because it may be a branch.

The integrated cross sections can be determined from the observed peak areas. The observed counts in a resonance peak can be decomposed into the following factors:

$$A_{\text{det}} = \Phi T_{\text{in}} C T_{\text{out}} \epsilon W, \quad (1)$$

where  $A_{\text{det}}$  is the number of fluorescence photons observed in the detector,  $\Phi$  is the incident photon flux per eV subtended by the target,  $T_{\text{in}}$  is the transmission probability of photons through any absorbing material before it reaches the fluorescing sample,  $C$  is the number of fluorescent photons per incident flux escaping the sample,  $T_{\text{out}}$  is the transmission probability of the fluorescing photons through all absorbing materials between the fluorescing sample and the detector,  $\epsilon$  is the efficiency of the detector, both intrinsic and geometric, and  $W$  is the angular dependence of the resonance. All of the factors on the right-hand side are dependent on the energy. The transmission probabilities were determined from the electronic attenuation coefficients as taken from the XCOM [11] database.

The calculation of  $C$  is described in Ref. [12].  $C$  accounts for the attenuation in the fluorescing material due to electronic and nuclear processes for the incident photon and for electronic processes for the fluorescent photon as well as the effect of Doppler broadening of the resonance. For thin targets, in which attenuation and Doppler effects are not significant, and ignoring less likely physical processes,  $C$  simplifies to

$$C \sim C_{\text{thin}} = N \int \sigma_{\text{NRF}} dE \quad (2)$$

where  $N$  is the number of sample nuclei per area and the energy integral represents the integrated cross section over the resonance for the NRF process. Thus,  $C$  is the quantity that is sensitive to the NRF integrated cross section.

The integrated cross sections were extracted by comparing the measured areas of the  $^{235}\text{U}$  and  $^{239}\text{Pu}$  peaks to the strengths of known NRF peaks. A ratio of two versions of Eq. (1), one for the known peak and one for the unknown peak, was formed:

$$\frac{C_x}{C_0} = \frac{A_{\text{det},x} \Phi_0 T_{\text{in},0} W_0 T_{\text{out},0} \epsilon_0}{A_{\text{det},0} \Phi_x T_{\text{in},x} W_x T_{\text{out},x} \epsilon_x}, \quad (3)$$

where the  $x$  and 0 denote quantities for the unknown and known resonances. As a result of forming this ratio of two very similar measurements, the extraction of  $C_x$ , the quantity sensitive to the unknown NRF strength, depends only on the relative transmissions, efficiencies and fluxes, which considerably reduces the systematic sensitivities. The angular dependence,  $W$ , depends on the spins of the initial and final states of the transition. Since the measurements do not determine the angular distribution of fluorescence emissions, the angular dependence was taken as an average of all possible dipole transitions given the angular momenta involved. The uncertainty in this correction was determined from the standard deviation of  $W$  for the possible dipole transitions. The average relative correction for  $W$  is small,  $\sim 1\%$ , with a  $\sim 6\%$  absolute

uncertainty on that correction. The ratio of detector efficiencies was determined through radiation transport modeling using the GEANT4 [13] framework. The ratio of the photon flux was determined through an energy-dependent flux calculation with MCNP [10].

The NRF resonances of  $^{235}\text{U}$  listed in Table I were determined by comparing to the observed strengths of the 1884-keV resonance of  $^{55}\text{Mn}$ . Measurements were conducted with two basic geometries, one with the manganese upstream of the uranium (Mn+HEU) and the other with the uranium upstream of the manganese (HEU+Mn). The strongest  $^{235}\text{U}$  line at 1733 keV was compared to the 1884-keV line of  $^{55}\text{Mn}$  in the Mn+HEU geometry. This geometry yields a smaller systematic uncertainty in the extracted cross section because one does not have to correct for the attenuation of the  $^{55}\text{Mn}$  line through the HEU of varying thickness. The strengths of the other  $^{235}\text{U}$  resonances were then determined relative to the 1733-keV resonance of  $^{235}\text{U}$  in the HEU+Mn geometry because of a significant statistical advantage compared to the Mn+HEU geometry. The strengths for both the HEU+Mn and Mn+HEU geometries were found to be consistent.

The Mn cross section was determined by a separate measurement. The ratio of peak counts following Eq. (3) for the 1884-keV line of  $^{55}\text{Mn}$  relative to the well-known 2211-keV line of  $^{27}\text{Al}$  was determined by measuring the NRF response of two similar mass and diameter manganese and aluminum disks. These measurements were motivated by the wide discrepancy in the data used in ENSDF [14] for the evaluated decay width of the 1884-keV state. This discrepancy would have dominated the uncertainties in the  $^{235}\text{U}$  NRF integrated cross sections. Our results of  $45.0 \pm 3.7$  eV·b for the integrated cross section is consistent with earlier measurements [15] after correcting for the ENSDF branching ratio, as well as two out of three measurements used to form the ENSDF evaluation.

For the  $^{235}\text{U}$  NRF lines, there are two pairs of lines that are associated with each other. These pairs of lines are indicated by the daggers  $\dagger$  and  $\ddagger$  in Table I. The energy separation of these pairs of lines is 46.2 keV, suggesting that the pair of transitions are generated by the excitation of the same level, but one decays to the ground state and the other to the 46.2 keV  $J^\pi = 9/2^-$  state of  $^{235}\text{U}$ . Similar pairing of transitions has also been observed in  $^{238}\text{U}$  and is discussed later in  $^{239}\text{Pu}$ . This observation provides strong circumstantial evidence that the origin of these lines is indeed  $^{235}\text{U}$ .

A different pairing of states and transitions is also possible. The photon line at 1733.6 keV can originate from the decay of the state at 1815.3 keV to the excited state of  $^{235}\text{U}$  at 81.7 keV. In this situation the line at 1687.3 keV would require a new state at that energy, without an observed partner for decay to the excited state at 46.2 keV. This alternative interpretation is less likely because of the change in structure of the state at 81.7 keV (positive parity) compared to the ground state rotational band (negative parity).

Starting with the hypothesis that there are states at 1815.3 and 1733.6 keV, the ratios for decay to the ground and first excited rotational states might be candidates for comparison to the Alaga rules for decay between states with  $K = 7/2$  as in the case of  $^{175}\text{Lu}$  where an octupole-quasiparticle band

is observed [16]. The same ratios were observed in  $^{175}\text{Lu}$  is expected. The regularity is not observed for the transitions in  $^{235}\text{U}$  implying a considerably different structure for the two excited states and, perhaps, also  $K$ -mixing.

The integrated cross sections listed in Table I for  $^{239}\text{Pu}$  were determined by comparing the intensities of the  $^{239}\text{Pu}$  peaks to the 2211-keV transition of  $^{27}\text{Al}$  and the known strength of that state,  $T_{1/2} = 26.4(7)$  fs [14]. To verify the accuracy of the ratio approach for Pu, the integrated cross sections of the resonances listed in Table I were determined via an absolute method. The measurements and simulation estimates were put into Eq. (1) and the integrated cross sections were deduced. The integrated cross sections for Pu from the absolute method are in agreement with those listed for Pu in Table I from the ratio method. The largest source of uncertainty in the cross sections for Pu was due to low statistics. Systematic as well as statistical uncertainties are included in Table I.

As discussed above for  $^{235}\text{U}$ , the energy difference between pairs of some of the Pu lines provides evidence that the above transitions are indeed associated with  $^{239}\text{Pu}$ . Pairs of lines are denoted in Table I by double asterisks \*\*. A proposed level at 2431.7(3) keV is populated with an incident photon and appears to decay via two branches: a 2431.7(3)-keV  $\gamma$ -ray directly to the ground state and a  $\gamma$ -ray 2423.5(3)-keV to the 7.861-keV level. Under these circumstances, the integrated cross section of the 2431.7(3)-keV level is 19(4) eV·b and has a branching ratio of 46(5)% to the ground state.

It is possible that the 2135-keV transition is a branch from a level at 2143.6(1) MeV. The energy difference is 8.6(3) keV, which is  $\sim 2\sigma$  larger than the known energy difference between the ground state and first excited state at 7.861 keV [14]. In this case, part of the strength of the 2143.6(1)-keV transition is associated with a direct transition to the ground state. In addition, part of the strength could be associated with a branch to the first excited state from a proposed level at  $\approx 2151$  keV. The remainder of the decay strength from the 2151.0(3)-keV level goes directly to the ground state via a 2151.0(3)-keV transition. The cross sections are calculated in these cases assuming only direct transitions to the ground state.

**Conclusion.** The process of NRF generates monochromatic photon lines that can be used for the unique identification of the isotopes of  $^{235}\text{U}$  and  $^{239}\text{Pu}$ . In the energy range studied there are nine lines observed in  $^{235}\text{U}$  and 12 lines observed in  $^{239}\text{Pu}$ . Some of the lines originate from single excited states that have significant branching ratios to the first excited rotational states of these isotopes. The unique energy of these rotational states also confirms the isotopes involved. The integrated cross sections of the observed transitions were determined to be as large as  $\approx 30$  eV·b. These states provide a practical means of detecting these isotopes for nonintrusive inspections [1,2].

While it was not possible to establish the spins and parities of the excited states, dominance of the dipole transition suggest the spins are the ground state spin  $\pm 1,0$ . In the case of  $^{235}\text{U}$ , the results are not consistent with the Alaga rules for branching ratios. In the case of  $^{239}\text{Pu}$ , the spin of the ground state is 1/2 and the mixing of  $K$ -values from Coriolis effects render it difficult to make any spin conclusions beyond the assumption of the dominance of dipole transitions. The energy of the states in  $^{239}\text{Pu}$  are close to where the  $M1$  scissors states are

observed in  $^{238}\text{U}$  suggesting the possibility that the states in  $^{239}\text{Pu}$  are  $M1$  and part of the “scissors mode.” Additional measurements would be required to test the validity of this possibility.

Further effort is required to determine the spin assignments of excited states and to establish the dynamics of the excitations involved. In addition, searching for new resonances at higher energies is critical. For some applications, higher energy resonances may provide a significant performance enhancement in practical systems exploiting NRF to detect special nuclear materials.

PNNL is operated for the U.S. Department of Energy (DOE) by Battelle Memorial Institute under Contract DE-AC06-76RLO 1830. PNNL’s contribution to this project was funded by the U.S. DOE Office of Defense Nuclear Nonproliferation, Office of Nonproliferation Research and Development. LLNL’s contributions were funded by the U.S. Department of Homeland Security Domestic Nuclear Detection Office (DHS/DNDO). This work performed under the auspices of the U.S. DOE by LLNL under Contract DE-AC52-07NA27344. Passport supported in part by DHS/DNDO, SPAWAR contract N66001-05-D-6011/0002 and N66001-07-D-0025/0001.

- 
- [1] W. Bertozzi and R. Ledoux, Nucl. Instrum. Methods Phys. Res. B **241**, 820 (2005).
  - [2] J. Pruet *et al.*, J. Appl. Phys. **99**, 123102 (2006).
  - [3] D. Slaughter *et al.*, UCRL-ID-155315 (2005).
  - [4] L. J. Schultz *et al.*, Nucl. Instrum. Methods Phys. Res. A **519**, 687 (2004).
  - [5] Konstantin N. Borozdin *et al.*, Nature **422**(6929), 277 (2003).
  - [6] J. Margraf *et al.*, Phys. Rev. C **42**, 771 (1990).
  - [7] A. Zilges *et al.*, Phys. Rev. C **52**, R468 (1995).
  - [8] H. H. Kneissl *et al.*, Prog. Part. Nucl. Phys. **37**, 349 (1996).
  - [9] R. F. Casten, *Nuclear Structure from a Simple Perspective* (Oxford University Press, Oxford, 1990).
  - [10] X-5 Monte Carlo Team, Monte Carlo Transport Code, LA-UR-03-1987 (2003).
  - [11] M. J. Berger *et al.*, XCOM: Photon Cross Section Database, National Institute of Standards and Technology, NBSIR 87-3597 (1998).
  - [12] F. R. Metzger, Prog. Nucl. Phys. **7**, 53 (1959).
  - [13] S. Agostinelli *et al.*, Nucl. Instrum. Methods Phys. Res. A **506**, 250 (2003).
  - [14] *Evaluated Nuclear Structure Data File* (Brookhaven National Laboratory, Upton, NY, 2003).
  - [15] W. J. Alston, H. H. Wilson, and E. C. Booth, Nucl. Phys. **A116**, 281 (1968); see also Nucl. Phys. **A139**, 713 (1968).
  - [16] Herzberg *et al.*, Phys. Rev. C **56**, 2484 (1997).